*Thermophysics and Aeromechanics*, *2022*, *Vol. 29*, *No. 4*

DOI: 10.1134/S0869864322040126

# Nucleation and structuring in aluminum and in AlSi12Cu2NiMg alloy with nanopaticle modifier under impact of electron-beam treatment*

**R. Lazarova[1], G.E. Georgiev[1], A.N. Cherepanov[2], and V. Dyakova[1]**

[1]*Balevsky Institute of Metals Science, Construction, and Technology along with the Center for Fluid Dynamics BAS, Sofia, Bulgaria*

[2]*Khristianovich Institute of Theoretical and Applied Mechanics SB RAS, Novosibirsk, Russia*

E-mail: ancher@itam.nsc.ru

(*Received February 1, 2022*; *revised March 19, 2022*; *accepted for publication March 22, 2022*)

The paper presents experimental and theoretical study of crystal nucleation and growth in aluminum and structure development in the aluminum melt after the introduction of a cubic-shaped nanoparticle modifier and using the electron-beam surface treatment method. The output of this study is the rate of solid phase nucleation as a function of TiCN nanoparticle size dispersed in molten aluminum. The numerical simulation of crystal structure growth for a sample of AlSi12Cu2NiMg alloy treated by electron beam was performed using the MAGMASOFT computer code.

**Keywords**: electron-beam treatment, nanoparticles, modifier, crystal structure.

## Introduction

The authors in previous papers [1 – 4] had demonstrated the way to producing the nanocomposite coating on aluminum or aluminum-alloy substrate through depositing the nanopowder on the surface with the following treatment using electron beam technology. The impact of the electron beam on the surface produces a melt where the nanoparticles are mixed with the melt. Besides, they work as a metal modifier and become the additional centers for crystallization. The liquid metal on the sample surface solidifies and this produces a high-dispersion nanobased composite coating. The diagram of electron-beam modification of an aluminum substrate is depicted in Fig. 1. This treatment improves the dispersion degree, increases the strength characteristics, micro hardness, and durability of the surface layer of the treated sample.

*Research was supported by project No. DN 07/16 financed by the Research Foundation of the Republic of Bulgaria and partly by the project No.121030500137-5 of the sate assignment of the Russian Ministry for Science and Education.

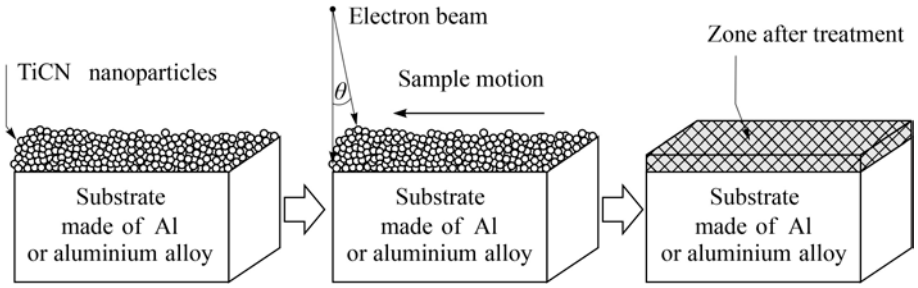


*Fig. 1.* Diagram for the process of substrate treatment with an electron beam.

The goal of this study is the investigation of the processes of nucleation and structuring in aluminum and in AlSi12Cu2NiMg alloy while introducing the TiCN nanoparticles. This problem statement accounts for several aspects: crystallization in the liquid zone of the treated substrate with the introduced refractory nanoparticles is nonuniform; the metal solidification in small volumes after surface treatment with a high energy flux has a high rate.

## 1. Nucleation process

In the process of cooling of liquid layers of aluminum (or AlSi12Cu2NiMg alloy) the introduced nanoparticles (NP) make a substrate work with crystallization centers. The nucleation rate depends on the NP size, their wetting parameter, atomic diameters of elements comprising the liquid metal composition, and on other physical and chemical characteristics of the liquid metal. The nanoparticles work as the nucleation centers for silicon phase and they supress the growth of eutectic silicon. Provided a high concentration of NP (however, below the coagulation limit) and a high wetting, this composition produces a more subtle dendrite (or globular) structure. Those new properties of the treated metal surface are due to the improved nanoparticle-modified microstructure and due to intensive electron beam treatment.

The recent years demonstrate a growth in publications on study of NP-in-melt effect on the crystallization-produced microstructure and the mechanical properties of the solidified metal [5–13]. The research found that the NP-containing microstructure is finer than the corresponding structure without NP [14–16]. This means that nanoparticle create a refining action on the crystallites. Another discovered effect was the modification of the dendrite surface with nanopowders [17]. These observations are supported by theoretical analysis that assumes blocking of alloy components diffusion by nanopowder during the solidification process [18].

The literature data disclose that the adding of NP increases the rate of nucleation (the formation of crystallization centers) while restricting the growth of dendrites and changing their morphology. For example, research [19, 20] revealed that the changes in microstructure during crystallization occur due to NP-induced suppression of Zn diffusion ahead of the dendrite axes and the growth rate of the apexes slows down. The mechanism of nucleation in liquid metal with addition of cubic nanoparticles was described in [21, 22].

### 1.1. Experiments

The samples of pure aluminum were surface-modified with cubic TiCN nanoparticles (the cube edge length $l_p$ was 40 nm — see Figs. 2 and 3) using the electron beam treatment. The test samples were parallelepipeds with the size of $20 \times 10 \times 10$ mm. The sample surface was preliminarily polished with the No. 1200 sandpaper and cleansed with ethyl alcohol and dried. Then the surface of sample was coated with a slurry: it was acrylic glass powder solved

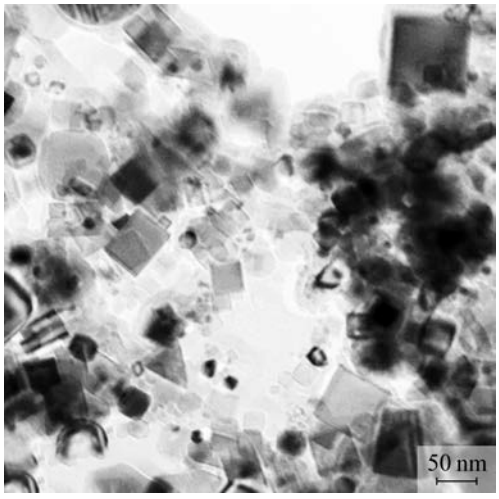


*Fig. 2*. General view for the morphology of TiCN nanoparticles.

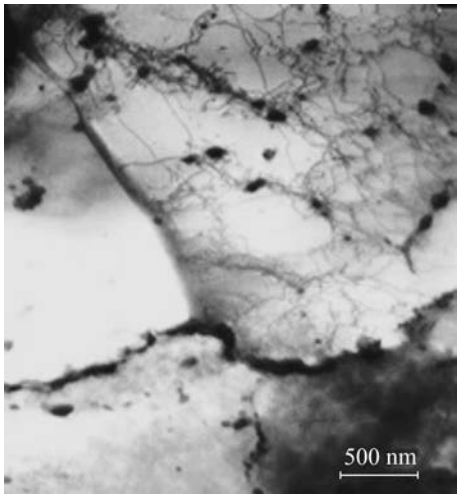


*Fig. 3*. Image of the microsection for a sample of Al modified with TiCN nanoparticles.

in three droplets of $CHCl_3$ solvent with the addition of TiCN nanopowder. The surface was coated with this slurry for two variants of surface concentration ($M_p$) — 0.015 and 0.03 mg/mm$^2$ — with a spatula until producing a smooth layer on the substrate. The electron-beam treatment was performed in Leybold Heraeus vacuum apparatus (EWS 300/15-60). The processing parameters were the following: the electron beam current $I$ = 18–25 mA, the sample displacement velocity $v$ = 0.5–5 cm/s, and the scanning frequency by electron beam $f$ = = 200–10 000 Hz. For all experiments, the acceleration voltage was $U$ = 52 kV, and the focusing current was $I_f$= 472 mA. The sample surface treatment was performed using annular scanning trajectory.

### 1.2. Theory

According to paper [23], the refractory NPs are the potential centers for crystallization: separate clusters are formed at NP surface which (under certain conditions) transform into solid-phase nuclei. As it was in papers [21, 22], we assume that the nucleus has a spherical segment shape attached to the surface of a cubic nanoparticle with the wetting angle in the range $0° < \theta < 90°$ (Fig. 4) and the contact spot has the diameter lower than the cubic particle edge length $l_p$, i.e., it is defined as $2R_c \sin\theta \le l_p$, where $R_c$ is the nucleus critical radius.

The rate of heterogeneous nucleation $J$ and the Gibbs' free energy $\Delta G^*$ in the melt with NP with account for size effect is defined by the formulas [21]:

$$J = n_p (12\pi D_0)/(l_a^4)\,(l_p/l_c)^2 R_c^{\,2}\,(1-\cos\theta)\exp\left[(-(E+\Delta G^*))/(k_B T)\right], \tag{1}$$

$$\Delta G^* = 1/3\,\pi\sigma_{12}^{\infty} R_0^{\,2}\,(1-6\delta/R_0)\,(1-\cos\theta)^2\,(2+\cos\theta), \tag{2}$$

where $n_p = m_p \rho/100\,\rho_p l_p^3$, $R_c \approx 2\sigma_{12}^{\infty}(1-2\delta/R_0)T_s/(\kappa\rho\Delta T)$, $T$ is the current temperature, $\sigma_{12}^{\infty}$ is the surface tension at the interface "nucleus–melt" at $2\delta/R_0 \to 0$, $m_p$ is the modifier mass fraction (wt. %), $\delta$ is the Tolman parameter that describes the size of interphase transition layer, $\Delta T$ is the subcooling, $T_s$ is the crystallization temperature, $\rho$ is the metal density, $\rho_p$ is the NP density, $\kappa$ is the crystallization heat, $l_a$ is the diameter of liquid metal atom, $l_c$ is the interatomic

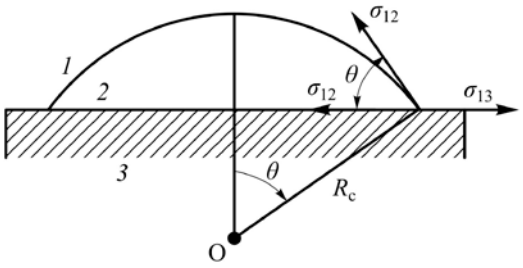


*Fig. 4*. Diagram of a nucleus on a flat wall of a nanoparticle.
*1* — melt, *2* — nucleus *3* — nanoparticle.

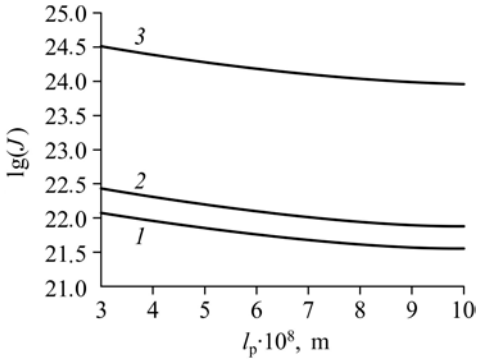


*Fig. 5*. Nucleation rate ($J$, $s^{-1}m^{-1}$) vs. nanoparticle size at parameter $2\delta/R_0 = 0$ (*1*), 0.007 (*2*), 0.05 (*3*) and for $M_p = 0.03$ mg/mm$^2$.

distance for the substrate, $k_B$ is the Boltzmann constant, $D_0$ is the empirical constant in the Arrhenius law, and $E$ is the activation energy for diffusion process in the aluminum melt.

The calculations for estimating the rate of homogeneous nucleation in aluminum melt were performed for the set of input data: $T_s = 933$ K, $\rho = 2350$ kg/m$^3$, $\kappa = 4.02\cdot10^5$J/kg, $D_0 = 10^{-7}$m$^2$/s, $E = 4.2\cdot10^{-20}$J, $\pi\sigma_{12}^{\infty} = 0.093$ J/m$^2$, $l_a = 2.86\cdot10^{-10}$m, $l_c = 4.235\cdot10^{-10}$m, $\rho_p = 5080$ kg/m$^3$, $k_B = 1.38\cdot10^{-23}$ J/K.

Figure 5 presents the dependency of nucleation rate on nanoparticle size at three different values of the Tolman parameter. Here the wetting angle $\theta$ was taken equal 10°, subcooling value is $\Delta T = 2$ K, and the surface density of nanoparticles $M_p = 0.03$ mg/mm$^2$. The analysis of calculated curves demonstrate that the low relative Tolman's parameter ($2\delta/R_0 < 0.01$) exhibits a low influence on the nucleation rate. Meanwhile, the reduction in the nanoparticle size (at a steady value of substrate material in the melt) enhances the rate, i.e., the smaller size of NP increases the nucleation rate.

The problem of nucleation rate for the AlSi12Cu2NiMg alloy is more complicated since the Tolman parameter for this case is determined by atomic diameters of elements comprising the melt, and development of different phase occurs at different levels of subcooling. Besides, we have to consider the behavior of grain growth in a metal melt including NP. The recent studies revealed that the presence of NP while metal crystallization both refine and modify the nucleus, that is, we observe a decrease in size and shape variation of the microstructure elements [17, 19, 24].

## 2. Processes of growth and modification

### 2.1. Growth and modification of dendrites

It was found in [19] that NPs reduce the effective diffusive capability of the dissolved component Zn in a fluid: they work as effective inhibitor of dendrite growth. The authors also discovered that NP additive alters the microstructure morphology: it changes from the dendrite to the hyper-branched structure with dispersed ends. The qualitative evaluation of the top branches of dendrites using the data from X-ray tomography (in cooperation with analytical calculations) demonstrated that the change in growth of dendrite structure is due to the fact that NPs reduce the effective solubility of dopant impurity in the liquid near the solid-liquid

interface. This restricts the redistribution of dissolved elements and increases their concentration at the dendrite tips: this creates the hyper-branched morphology of grains.

### 2.2. Growth and modification of silicon crystals

It was found in [25 – 27] that NPs are useful for control of the eutectic phase growth of Si during melt solidification. It was also discovered [28, 29] that NPs of $Al_2O_3$ and TiCN inhibit this growth of Si eutectic phase due to placing the NPs at the Al/Si interface: this improves the dispersion of the eutectic phase.

The qualitative microscopic analysis of AlSi12Cu2NiMg samples (Figs. 6*a* and 6*b*) demonstrated that the nanoparticle modifiers are beneficial in refining the primary and eutectic crystals in the treated layer.

## 3. Modeling of structuring process in a AlSi12Cu2NiMg alloy sample after electron-beam treatment using the MAGMASOFT code

The 3D diagram of AlSi12Cu2NiMg alloy sample (used in our experiments) is plotted in Fig. 7. The EB-treated surface layer has a uniform set of reference points marked as T1, T2, ..., T10. The diagram was generated with the geometry generator of the MAGMASOFT code version 5.5.0.1. The process of surface layer heating was arranged and performed under the condition described above (section 1.1) using the code tools. The code gives the solution of the sample temperature field that is shown in Fig. 8. The temperatures at the control points placed according to Fig. 7 are shown in Fig. 9 using a color mapping. Here the temperatures in control points are simulated with the MAGMASOFTc code. These plots demonstrate the temperature evolution during the period of 1.33 s (the duration of electron beam scanning

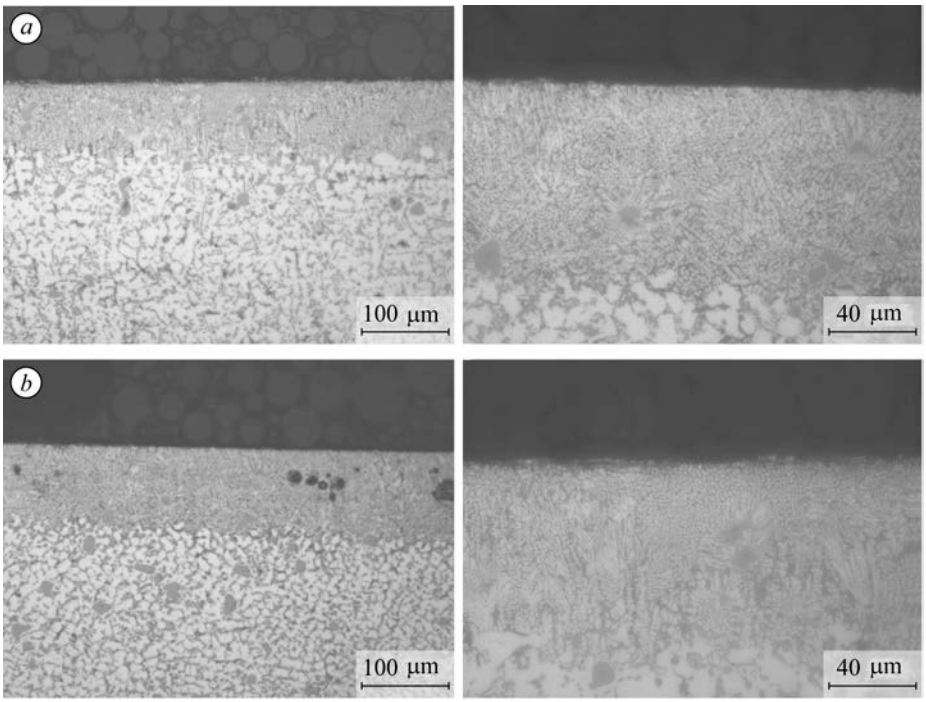


*Fig. 6*. Microstructure of surface layer from samples with surface NP concentration 0.015 mg/mm$^2$ (*a*) and 0.03 mg/mm$^2$ (*b*).

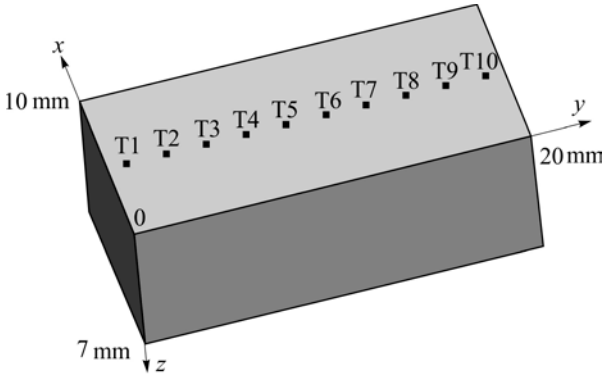


*Fig. 7.* Diagram for AlSi12Cu2NiMg alloy sample subjected to electron beam treatment (reference points are depicted).

over the sample surface). The graphs show also the liquidus and solidus temperatures of the AlSi12Cu2NiMg alloy. This tracks down the dynamics of the process: we can know the duration of staying in the two-phase zone for any local area (when the area temperature is between the solidus and liquidus). Modeling shows the time when the metal was liquid and then solidified. This is the time for forming the microstructure and this is much shorter than the entire time of treatment.

We also used a phenomenology criterion "grain size" offered by the code for forecasting the grain sizes in the final layer after electron beam treatment. Figure 10 presents the magnified segment of the vertical cross section in this layer. The color coding was used for visualization of the grain size distribution. One can see that the grain size at the surface is about 1.0 μm, but at the higher depths it becomes about ~1.85 μm — this means the generation of extremely fine-grain microstructure. The bigger grains are in the middle of cross section (yellow and red colors), meanwhile a tendency to smaller grains (blue color) is observed near the top and bottom surfaces of the tested layer: this is due to a higher rate of cooling at the sample surface.

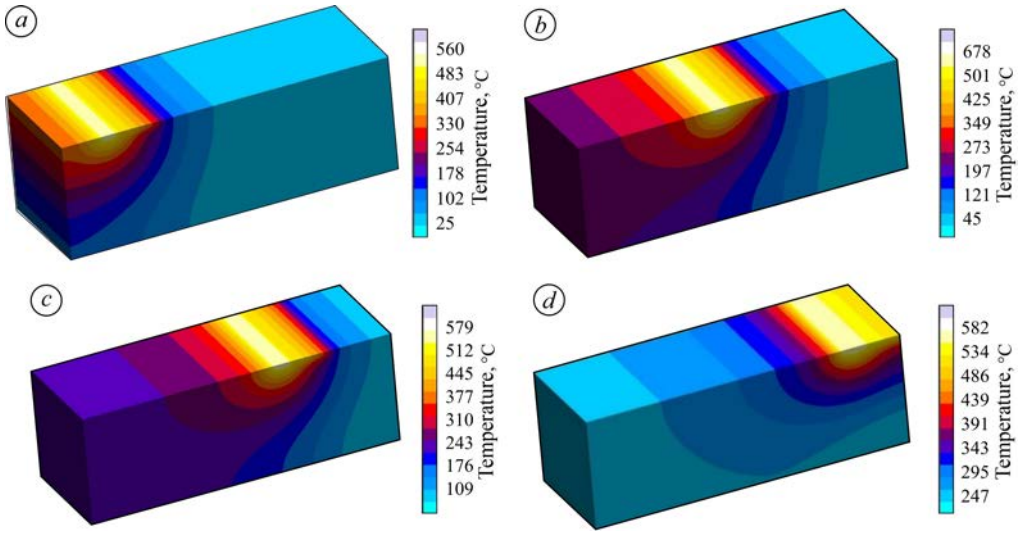


*Fig. 8.* Temperature field at different times during sample heating.
$t$ = 0.262 s (*a*), 0.782 s (*b*), 0.912 s (*c*), and 1.172 s (*d*).

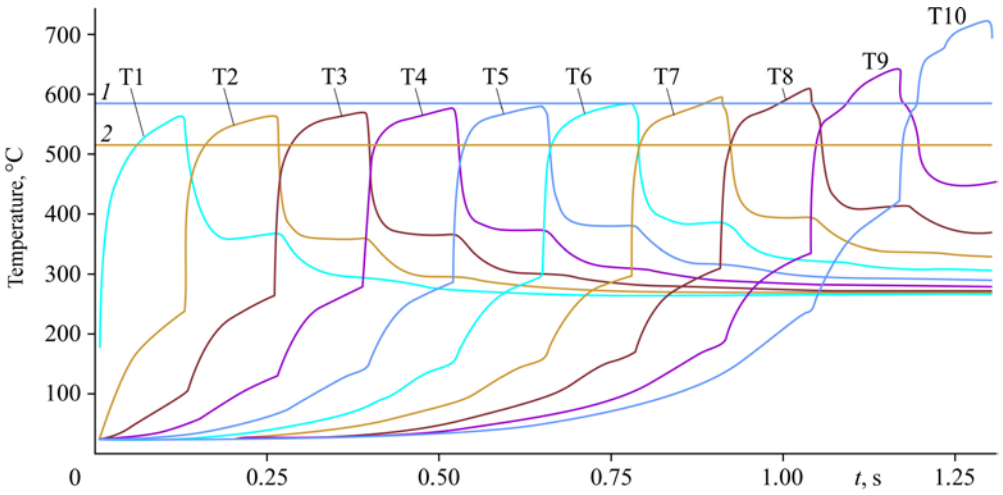


*Fig. 9.* Temperature evolution curves at reference points for a sample displacement with the velocity $v$ = 15.4 mm/s.
*1* — liquidus temperature, *2* — solidus temperature.

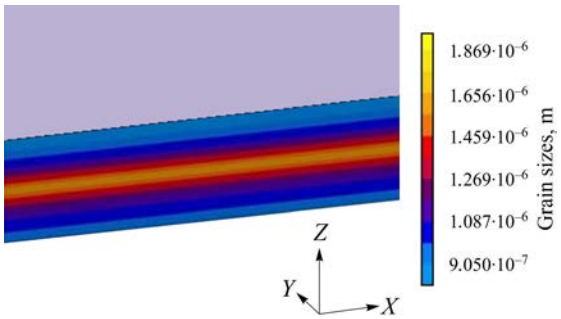


*Fig. 10.* Grain size within the surface layer of the AlSi12Cu2NiMg sample after EB treatment.

*Fig. 11.* Grain size distribution over the transversal cross section of the treated layer (axis *Z*).

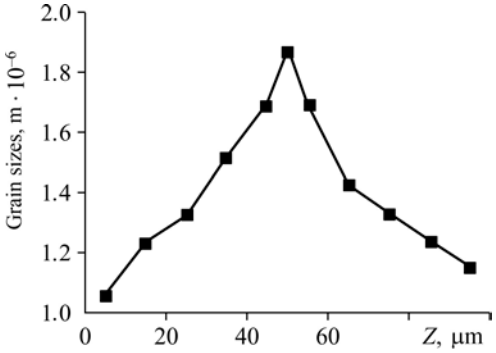


Figure 11 illustrates the distribution of the crystal grain size in the metal layer cross section. Note that these simulation results for grain size are close to the experimental data (see Fig. 10).

## Conclusion

When the liquid layers of aluminum or AlSi12Cu2NiMg alloy are cooled, the nanoparticles within the layer serve as substrates for generating the crystallization centers. The rate of nucleation depends on the size of nanoparticles and the atomic diameters of elements of the liquid metal and from other physical and chemical parameters. In theory, this rate was

determined for pure aluminum. It was demonstrated that the introduced nanoparticles refine the primary phase grains and become the nucleation centers for the silicon phase — this hinders the eutectic silicon growth. The improvement for the treated layer properties can be explained by improvement in the fine-grain structure of the metal and by high-energy electron beam treatment.

The authors are grateful to their colleagues from the Physics Technology Lab from the institute of Electronics of the Bulgarian Academy of Sciences for sample testing.

## References

1. **R. Lazarova, R. Dimitrova, Y. Murdjeva, St. Valkov, and P. Petrov,** Layers obtained on aluminum by nanopowder deposition and subsequent electron beam scanning, Materials and Manufacturing Processes. 2018, Vol. 33, No. 10, P.1128–1132.
2. **L. Anestiev, R. Lazarova, P. Petrov, V. Dyakova, and L. Stanev,** On the strengthening and the strength reducing mechanisms at aluminium matrix composites reinforced with TiCN nano-sized particulates, Phil. Magazine, 2019, Vol. 101, Iss. 2, P.129–153.
3. **S. Valkov, R. Bezdushnyi, R. Lazarova, R. Dimitrova, and P. Petrov,** Surface modification of Al substrate with TiCN nanopowder by electron-beam treatment, AIP Conf. Proceedings, 2019, Vol. 2075, Iss. 1, P. 160017-1–160017-5.
4. **R. Lazarova, S. Valkov, V. Dyakova, and P. Petrov,** Layers obtained on TiCN aluminum nanocomposites by electron-beam treatment, Intern. Conf. on Novel Functional Materials. IOP Conf. Series: Materials Sci. and Engng., 2020, Vol.733, P. 012017-1–012017-9.
5. **R. Lazarova, N. Bojanova, R. Dimitrova, I. Panov, and V. Manolov,** Influence of nanoparticles introducing in the melt of aluminum alloys on castings microstructure and properties, Intern J. Metalcasting, 2016, Vol. 10, Iss. 4, P. 466–476.
6. **A.N. Cherepanov, A.M. Orishich, V.E. Ovcharenko, A.G. Malikov, V.O. Drozdov and A.P. Pshenichnikov,** Influence of modifying nanoadditives on the properties of a multilayer composite coating obtained by laser surfacing, Physics of Metals and Metallography, 2019, Vol. 120, No.1, P. 101–106.
7. **H. Dieringa,** Properties of magnesium alloys reinforced with nanoparticles and carbon nanotubes: a review, J. Mater. Sci., 2011, Vol. 46, No. 2, P. 289–306.
8. **A.N. Cherepanov, V.E. Ovcharenko, G. Liu, and L. Xao,** Modifying structure and properties of nickel alloys by nanostructured composite powders, Thermophysics and Aeromechanics, 2015, Vol. 22, No. 1, P. 127–132.
9. **B.F. Schultz, J.B. Ferguson, and P.K. Rohatgi,** Microstructure and hardness of $Al_2O_3$ nanoparticle reinforced Al-Mg composites fabricated by reactive wetting and stir mixing, Mater. Sci. Engng., 2011, Vol. 530, P. 87–97.
10. **X.Y. Jia, S.Y. Liu, F.P. Gao, Q.Y. Zhang, and W.Z. Li,** Magnesium matrix nanocomposites fabricated by ultrasonic assisted casting, Inter. J. Cast Metal Res., 2009, Vol. 22, No. 4, P. 196–199.
11. **L. Katsarou, M. Mounib, W. Lefebvre, S. Vorozhtsov, M. Pavese, C. Badini, J.M. Molina-Aldareguia, C.C. Jimenez, M.T.P. Prado, and H. Dieringa,** Microstructure, mechanical properties and creep of magnesium alloy Elektron 21 reinforced with AlN nanoparticles by ultrasound-assisted stirring, Mater. Sci. Engng, 2016, Vol. 659, P. 84–92.
12. **D.K. Wang, M.P. De Cicco, and X.C. Li,** Using diluted master nanocomposites to achieve grain refinement and mechanical property enhancement in as-cast Al-9Mg, Mater. Sci. Engng., 2012, Vol. 532, P. 396–400.
13. **H. Men, B. Jiang, and Z. Fan,** Mechanisms of grain refinement by intensive shearing of AZ91 alloy melt, Acta Mater., 2010, Vol. 58, No. 19, P. 6526–6534.
14. **W. Mirihanage, W.W. Xu, J. Tamayo-Ariztondo, D. Eskin, M. Garcia-Fernandez, P. Srirangam, and P. Lee,** Synchrotron radiographic studies of ultrasonic melt processing of metal matrix nano composites, Mater. Lett., 2016, Vol. 164, P. 484–487.
15. **X.Y. Jia, S.Y. Liu, F.P. Gao, Q.Y. Zhang, and W.Z. Li,** Magnesium matrix nanocomposites fabricated by ultrasonic assisted casting, Inter. J. Cast Metal Res., 2009, Vol. 22, No. 4, P. 196–199.
16. **D.K. Wang, M.P. De Ciccom, and X.C. Li,** Using diluted master nanocomposites to achieve grain refinement and mechanical property enhancement in as-cast Al-9Mg, Mater. Sci. Engng., 2012, Vol. 532, P. 396–400.
17. **L.Y. Chen, J.Y. Peng, J.Q. Xu, H. Choi, and X.C. Li,** Achieving uniform distribution and dispersion of a high percentage of nanoparticles in metal matrix nanocomposites by solidification processing, Scripta Mater., 2013, Vol. 69, No. 8, P. 634–637.
18. **R. Daudin, S. Terzi, P. Lhuissier, J. Tamayo, M. Scheel, N. Hari Babu, D.G. Eskin, and L. Salvo,** Particle-induced morphological modification of Al alloy equiaxed dendrites revealed by sub-second in situ microtomography, Acta Mater., 2017, Vol. 125, P. 303–310.

19. **L.Y. Chen, J.Q. Xu, H. Choi, H. Konishi, S. Jin, and X.C. Li,** Rapid control of phase growth by nanoparticles, Nat. Commun., 2014, Vol. 5, Iss. 1, P. 3879.
20. **E. Guo, S. Shual, D. Kazantsev, S. Karagadde et al.** The influence of nanoparticles on dendritic grain growth in Mg alloys, Acta Materialia, 2018, No. 152, P. 127–137.
21. **A.N. Cherepanov, V.K. Cherepanova, V. Manolov, and L. Yovkov,** On crystallization of a metal inoculated with nanoparticles, J. Physics: Conf. Series., 2018, Vol. 1115, P. 042042-1 – 042042-7.
22. **A.N. Cherepanov, V.K. Cherepanova and V. Manolov,** Heterogeneous nucleation and growth of a solid in a nanomodified alloy, J. Crystal Growth, 2019, Vol. 527, P.125251-1–125251-4.
23. **P.A. Rebinder,** Qualitative Steel, 1939, No. 3, P. 31–34.
24. **P.D. Jiang and J.K. Yu,** Simultaneous refinement and modification of the eutectic Si in hypoeutectic Al–Si alloys achieved via the addition of SiC nanoparticles, J. Mater. Researches Technol., 2019, Vol. 8, No. 3, P. 2930 – 2943.
25. **L.Y. Chen, J.Q. Xu, and X.C. Li,** Controlling phase growth during solidification by nanoparticles, Mater Res. Lett., 2015, Vol. 3, No. 1, P. 43 – 49.
26. **K. Wang and H.Y. Jiang,** Nanoparticle-inhibited growth of primary aluminum in Al–10Si alloys, Acta Mater, 2016, Vol. 103, P. 252–263.
27. **M. Bozhanova, V.K. Manolov, R.N. Dimitrova, R.L. Lazarova, and A.N. Cherepanov,** Improvement of quality of aluminum alloy slab through nano-modifiction, Tyazholoe Mashinostroenie, 2014, No. 6, P. 2 – 6.
28. **H. Choi and X. Li,** Refinement of primary Si and modification of eutectic Si for enhanced ductility of hypereutectic Al–20Si–4.5Cu alloy with addition of $Al_2O_3$ nanoparticles, J. Mater. Sci., 2012, Vol. 47, No. 7, P. 3096 –3102.
29. **K. Wang and H.Y. Jiang,** Microstructure and mechanical properties of hypoeutectic Al–Si composite reinforced with TiCN nanoparticles, Mater Des., 2016, No. 95, P. 545 –554.